Dual-Nitrogen-Source Engineered Fe-Nx Moieties as A Booster to Oxygen Electroreduction

Journal:	*Journal of Materials Chemistry A*
Manuscript ID	TA-ART-02-2019-001953.R1
Article Type:	Paper
Date Submitted by the Author:	22-Mar-2019
Complete List of Authors:	Wang, Dan; Harbin Institute of Technology Xiao, Lihui; Harbin Institute of Technology Yang, Peixia; Harbin Institute of Technology, Department of Chemistry and Chemical Engineering Xu, Zhengrui; Virginia Tech Lu, Xiangyu; Zhuhai Coslight Battery Co., Ltd. Du, Lei; Harbin Institute of Technology Levin, Oleg; St. Petersburg State University Ge, Liping; Harbin Institute of Technology Pan, Xiaona; Harbin Institute of Technology; Virginia Tech Zhang, Jinqiu; Harbin Institute of Technology An, Maozhong; Harbin Institute of Technology

ARTICLE

Dual-Nitrogen-Source Engineered Fe-Nx Moieties as A Booster to Oxygen Electroreduction

Received 00th January 20xx,
Accepted 00th January 20xx

DOI: 10.1039/x0xx00000x

Dan Wang,[a] Lihui Xiao,[a] Peixia Yang,*[a] Zhengrui Xu,[b] Xiangyu Lu,[c] Lei Du,*[a] Oleg Levin,[d] Liping Ge,[a] Xiaona Pan,[a, b] Jinqiu Zhang[a] and Maozhong An[a]

Metal-air batteries, particularly Zn-air battery, have triggered considerable enthusiasm of communities due to the highly theoretical power density. Developing highly active, cost-effective and alternative non-precious metal catalysts towards the oxygen reduction reaction (ORR) is pivotal for popularizing zinc-air batteries. The rational design and synthesis of this type of catalysts is thus critical, which, however, is still challenging to control the well-defined active sites as people expect. Herein, we report a dual-nitrogen-source mediated route to synergistically control the formation of active Fe-Nx moieties that are embedded in the carbon matrix. The facilely controlled coordination structures of precursors by dual-nitrogen-source approach is revealed as a key role in this report. Impressively, the optimized dual-nitrogen-source derived catalyst (i.e. Fe-N-C-800) presents prominently enhanced ORR activity with a half-wave potential at 0.883 V in alkaline electrolyte, higher by 32 mV and 72 mV than those derived from individual nitrogen source, which is also further evaluated in primary Zn-air batteries. The enhanced ORR activity of Fe-N-C-800 is attributed to the rich Fe-Nx active sites derived from the dual-nitrogen-source approach.

Introduction

As one of the most promising energy conversion devices, metal-air batteries have triggered extensive research interest due to their low cost and high energy density. Compared with lithium-air batteries, zinc-air batteries are more stable towards moisture and air, resulting in a simpler manufacturing process in practical applications.[1] However, the sluggish cathodic oxygen reduction is one of the most urgent challenges for the development of zinc-air batteries.[2,3] To date, precious metal group materials, especially platinum and its alloys, have been considered as the most efficient electrocatalysts for oxygen reduction reaction.[4-7] However, the scarce resource, high cost and inferior methanol tolerance significantly limit their large-scale commercial applications.[8,9] A promising alternative is to replace the precious metal materials, i.e., developing non-precious metal catalysts (NPMCs), which have been intensively focused on in the past years.[10-14]

Among the various alternative NPMCs, transition metal- and nitrogen- doped carbon materials (i.e. TM-N-Cs, M=Fe, Co, Cu, Mn, Ni, etc.) have been generally regarded as the most promising candidates to supersede precious metal catalysts.[15-21] Recently, the iron-based materials have attracted extensive attention on account of their superior ORR activity compared with other TM-N-Cs catalysts.[22-24] To date, the Fe-Nx moieties embedded in carbon matrix are generally considered as vital active sites for ORR processes,[25-27] which, however, are challenging to be controlled.[28,29] In such moieties, the nitrogen-containing ligands were proved to effectively anchor metals and avoid metal agglomeration during pyrolysis by particular coordination and steric hindrance effects.[30,31] These results indicate that nitrogen is pivotal in the formation of active Fe-Nx moieties. In order to well control the Fe-Nx active sites during pyrolysis and obtain efficient ORR catalysts, well-defined regulation of the coordination structure of the precursors is required.[30,32,33] In this regard, optimized nitrogen precursors are helpful to achieve these goals. For example, 1,10-Phenanthroline (Phen) as one of the typical nitrogenous ligands was helpful to facilely form a stable complex coordinated with Fe^{2+} at room temperature.[34,35] Due to the strong hexadentate coordination between Fe^{2+} and Phen, dominant Fe-Nx moieties might be prospectively generated as much as possible after pyrolysis because of effective anchoring and distribution of the iron atom in the target products.[35] On the other hand, Zelenay et al.[36] recently prepared highly efficient $Fe-N_4$ active sites using both polyaniline and cyanamide as nitrogenous precursors, which demonstrates that the dual nitrogen sources are useful in modulating Fe-Nx moieties.

Based on the above, although Phen has strong affinity with iron, the nitrogen content is low. Therefore, it is reasonable to introduce another abundant nitrogen resource to synergistically enhance well-defined Fe-Nx moieties with high density. To this end, urea is a desirable nitrogen precursor,

---

[a] MIIT Key Laboratory of Critical Materials Technology for New Energy Conversion and Storage, School of Chemistry and Chemical Engineering, Harbin Institute of Technology, Harbin, 150001 China. *E-mail: yangpeixia@hit.edu.cn; lei.du@hit.edu.cn
[b] Department of Chemistry, Virginia Tech, Blacksburg, VA 24061, USA
[c] ZhuHai Coslight Battery Co., Ltd., ZhuHai, 519180, China.
[d] St. Petersburg State University, 7/9 Universitetskaya Nab., St. Petersburg, 199034, Russian Federation.

Electronic Supplementary Information (ESI) available: Additional SEM, BET, XPS, CV tests and video S1. See DOI: 10.1039/x0xx00000x which has been widely used in designing and synthesizing nitrogen doped materials.[37,38] Importantly, the molecular size of urea is much smaller than Phen, leading to easy access of urea into small spaces.

Herein, we report a dual-nitrogen-source (big phen molecules and small urea molecules) route to synergistically achieve well-defined Fe-Nx moieties via one-step pyrolysis and conventional post-acid-treatment. Such engineered active sites lead to remarkably enhanced ORR activity compared with those using mono-nitrogen source. Impressively, the optimized Fe-N-C-800 catalyst presented a half-wave potential at as high as 0.883 V in alkaline electrolyte. Compared with the commercial Pt/C catalyst, the Zn-air battery with Fe-N-C-800 catalyst at cathode exhibits much more stable platform and higher specific capacity of 744 mAh·g_{Zn}^{-1} The improved ORR performance is attributed to rich density of the active Fe-Nx moieties from regulated coordination structures in precursors by dual-nitrogen-source. Importantly, the dual-nitrogen-source mediated approach is theoretically universal for other TM-N-Cs, shedding a light on design and synthesis of non-precious metal ORR catalysts.

Experimental

Synthesis of catalysts

The carbon precursors were initially leached by acids to remove impurities and introduce abundant functional groups. Briefly, 4g of Ketjen Black (EC 300J) was dispersed in 6 M HNO_3 under stirring, which was then refluxed at 80 °C for 6 h. After that, the obtained suspension was collected by centrifuging and washed for several times until pH=7. The obtained Ketjen Black (EC 300J) (denoted as KB) was dried in vacuum at 65 °C for 24 h.

0.5 mmol (99.4 mg) of $FeCl_2 \cdot 4H_2O$ and 1.5 mmol (270.3 mg) of Phen were dissolved in a mixture of ethanol and ultrapure water under continuously stirring. The solution turned blood red immediately, indicating that the Fe-Phen complex was successfully formed. Then, 2 g of urea and 400 mg of KB were added into the blood red solution followed by stirring for 2 h and dried in vacuum at 60 °C for overnight. In order to ensure that the precursors were mixed uniformly, the obtained solid was moved to an agate mortar and grinded for 10 min.

One-step pyrolysis was employed to synthesize the TM-N-C catalysts. The precursors were placed in a tube furnace and pyrolyzed at 800 °C for 1 h with a ramp rate of 5 °C min^{-1} under H_2/Ar (5%:95%) atmosphere. The obtained product was leached in 0.5 M H_2SO_4 at 80 °C for 6 h to remove the unstable Fe species followed by washing and centrifugation. After drying in vacuum at 65 °C for 24 h, the prepared catalyst was denoted as Fe-N-C-800. For comparison, samples using individual N source including Phen and urea, and the sample using dual N source without iron precursors were synthesized in similar procedures, which are denoted as Fe-Phen-C, Fe-Urea-C and N-C, respectively. Moreover, the optimization of the ratios of the precursors including Fe, Phen, urea and KB has been discussed in the ESI (Fig. S1). In addition to Fe-N-C-800, the pyrolyzed samples at 700 °C (Fe-N-C-700) and 900 °C (Fe-N-C-900) were prepared to investigate the pyrolysis temperature. The optimization of temperature at 800 °C has been discussed in the ESI (Fig. S2-S7).

Physical Characterization

The morphology of as-prepared materials was characterized by scanning electron microscopy (Quanta 200FEG) and transmission electron microscopy (FEI Talos F200x) operating at 200 kV. The X-ray diffraction (XRD) patterns were collected on a Bruker D8 diffractometer with Cu Kα (1.5406 Å) radiation. Fe K-edge extended X-ray absorption fine structure (EXAFS) experiments were performed at beamline 20-BM-B, Advanced Photon Source, Argonne National Laboratory (ANL). Raman spectra were recorded by a Raman spectrometer (HR800, JY Company) with 457.9 nm laser. The Brunauer-Emmett-Teller (BET) surface area and pore size distribution were examined by recording nitrogen adsorption-desorption isotherms on a gas adsorption analyzer (Bei Shi De 3H-2000PS1). X-ray photoelectron spectroscopy (XPS) measurements were measured by Physical Electronics PHI model 5700 instrument with Al Kα radiation (1486.6 eV). Binding energy of all samples was calibrated by setting the measured binding energy of C1s to 284.8 eV. The inductively coupled plasma optical emission spectrometry (ICP-OES, Agilent 7700 instrument) was employed to determine the final Fe contents in the catalysts.

Electrochemical measurements

All the electrochemical measurements were carried out in a three-electrode system controlled by a CHI760E electrochemical workstation at room temperature using Hg/HgO with 1 M KOH solution or saturated calomel electrode (SCE) as the reference electrodes (depends on alkaline or acidic electrolytes) and Pt plate as the counter electrode. All the potentials were reported with respect to the reversible hydrogen electrode (RHE) according to the equations: E (RHE) = E (Hg/HgO) + 0.889 V in alkaline electrolyte and E (RHE) = E (SCE) + 0.305 V in acidic electrolyte. A glassy carbon rotating disk electrode (RDE) with a diameter of 5 mm (geometric area: 0.19625 cm^2) was used as the working electrode. The catalyst ink was prepared in the following procedures: 5 mg of catalyst was firstly dispersed in 1 ml of solution containing 400 µl of isopropyl alcohol, 560 µl of ultrapure water and 40 µl of 5 wt% Nafion solution (Du-Pont); then the suspension was sonicated for 1 h to form a homogeneous catalyst ink. The catalyst loading on the working electrode was controlled at 0.459 mg cm^{-2} in 0.1 M KOH or 0.611 mg cm^{-2} in 0.1 M $HClO_4$, while the loading of commercial Pt/C (20 wt%) was 0.255 mg cm^{-2} (i.e. 51 μg_{Pt} cm^{-2}).

The polarization curve test was carried out in N_2- or O_2-saturated 0.1 M KOH solution with a scan rate of 10 mV s-1 from 1.2 V to 0.2 V. The ORR polarization curves were also recorded with a rotating rate ranging from 900 to 2500 rpm on RDE. The electron transfer number (*n*) was calculated according to the Koutecky-Levich equation:

$$\frac{1}{j}=\frac{1}{j_{\mathrm{L}}}+\frac{1}{j_{\mathrm{K}}}=\frac{1}{B\omega^{\frac{1}{2}}}+\frac{1}{j_{\mathrm{K}}}$$

$$B=0.2nFC_{O}D_{O}^{\frac{2}{3}}v^{-\frac{1}{6}}$$

where j is the measured current density (mA cm^{-2}), j_L and j_K are the diffusion-limited and kinetics current densities (mA cm^{-2}), respectively, ω is the rotation rate of the RDE (rpm), F is the Faraday constant (96485 C mol^{-1}), C_O is the bulk concentration of O_2 in 0.1 M KOH (1.2×10^{-6} mol cm^{-3}), D_O is the diffusion coefficient of O_2 in the solution (1.9×10^{-5} cm^2 s^{-1}), and v is the kinematic viscosity of the electrolyte (0.01 cm^2 s^{-1}).

The specific kinetic current density was calculated from the K-L equation:

$$j_K = \frac{j_L \times j}{j_L - j}$$

In addition, rotating ring-disk electrode (RRDE) tests were employed to evaluate the hydrogen peroxide yield (H_2O_2%) and the electron transfer number (n) according to the equations as follows:

$$H_2O_2(\%) = 200\frac{I_R / N}{I_D + I_R / N}$$

$$n = 4\frac{I_D}{I_D + I_R / N}$$

where I_D and I_R are disk and ring current, respectively, N is the collection efficiency of ring current (37%).

The catalyst was evaluated in a laboratorial Zn-air battery at room temperature. The air cathode was prepared in the following procedures: Fe-N-C-800 (2.5 mg), acetylene black (1 mg), activated carbon (4 mg), and Nafion (5 wt%, 8 μL) were dispersed in 200 μL of isopropyl alcohol, which was then sonicated for 30 min to form a homogeneous catalyst ink. Ni foams as the substrate were immersed in 1 M HCl solution and then washed with ethanol and ultrapure water. The catalyst ink was dropped onto the Ni foam with a mass loading of 2 mg cm^{-2} followed by drying in vacuum at 60 °C for 24 h. A commercial gas diffusion layer was used as a backing layer next to the Ni foam-based catalyst layer to make gas accessible and prevent electrolyte leakage. For comparison, the 20% Pt/C was employed as catalyst layer with the same loading. A polished zinc foil was used as the anode, and 6 M KOH solution was employed as the electrolyte. The polarization curves test was collected by a CHI760E electrochemical workstation. The galvanostatic discharge test at various current densities (5 mA cm^{-2}, 10 mA cm^{-2} and 25 mA cm^{-2}) was performed in the LAND CT2001A testing system.

Results and discussion

The synthesis of typical Fe-N-C-800 catalyst is illustrated in Scheme 1 (detailed molecular structures of Phen, Fe-Phen and urea are presented in Fig. S8). Briefly, Fe salt precursor and Phen were firstly dissolved in a mixture of ethanol and ultrapure water at room temperature to form a stable complex due to the strong coordination interaction between the iron and nitrogen in Phen. Then, moderate quantity of urea and pretreated KB were added into the solution under continuous stirring. The mixed precursors were subsequently pyrolyzed at 800 °C for 1 h followed by acid leaching to obtain the final catalyst sample. As discussed in the introduction, Phen serves as nitrogenous ligand to build strong coordination bond with Fe; on the other hand, the coordinated three ligand Phen molecules around iron are large, leading to steric hindrance effect and efficient protection of Fe atom from aggregation. Importantly, the secondary N source, urea, is much smaller so that urea could insert into the space of the Fe-Phen complex. This synergy of dual nitrogen sources is potentially advantageous to introduce much more nitrogen, generate more Fe-N bonds and provide higher active site density towards ORR. These hypotheses will be confirmed in the following contents.

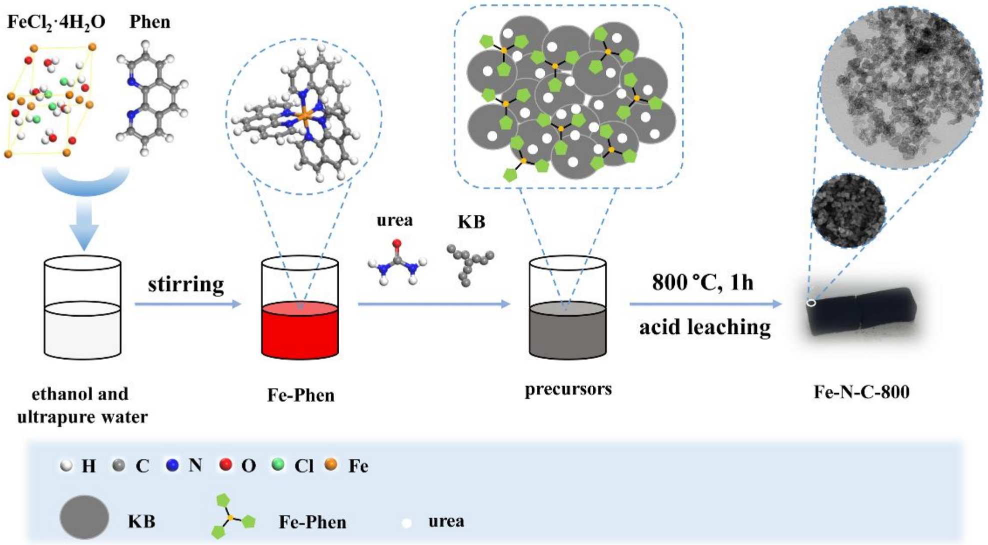

Scheme 1 Schematic illustration of the procedures used to synthesize Fe-N-C-800.

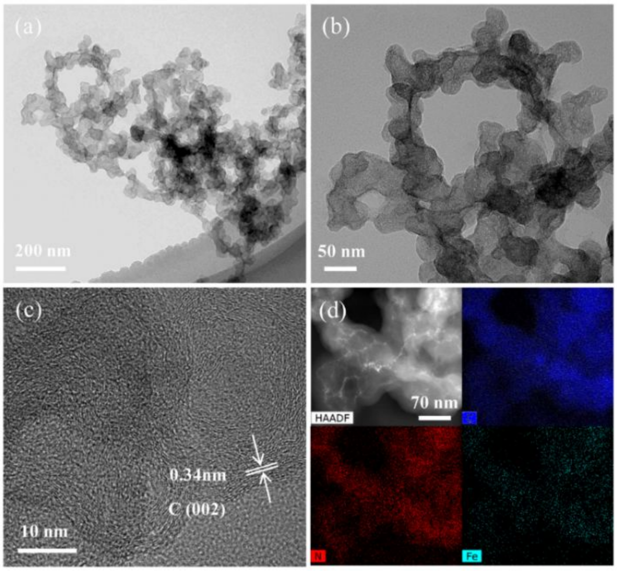

Fig. 1 (a, b) TEM images, (c) HRTEM image and (d) HAADF-STEM images of Fe-N-C-800 and corresponding elemental mapping images of C, N, Fe.

The scanning electron microscopy (SEM) images of precursor KB and Fe-N-C-800 are presented in Fig. S9 in the ESI. Obviously, Fe-N-C-800 after pyrolysis well keeps the morphology of KB. Generally, both of them present a granular-like morphology with a particle size distribution of about 50 nm. Further, the transmission electron microscopy (TEM) images of Fe-N-C-800 shows no obvious particles of Fe-containing species (Fig. 1a and b). In addition, as shown in Fig. 1c, the high-resolution TEM (HRTEM) image shows the lattice fringe with a spacing of 0.34 nm, which could be assigned to graphite (002) facet, further confirming the absence of highly crystalline Fe-containing species in the Fe-N-C-800. High-angle annular dark-field scanning transmission electron microscopy (HAADF-STEM) and related elemental mapping (Fig. 1d) demonstrate the presence of C, N, and Fe elements that distribute uniformly throughout the Fe-N-C-800 sample. Based on the above facts, it can be hypothesized that the dense and uniform Fe element does not exist in the form of big Fe particles, which might primarily coordinated with the generally existed N elements, i.e. Fe-Nx moieties.

To further characterize the dual-nitrogen-source derived materials, the crystal structure was characterized by X-ray diffraction (XRD). As shown in Fig. 2a, all catalysts (N-C without Fe source, Fe-Urea-C without Phen source, Fe-Phen-C without urea source and Fe-N-C-800) exhibit two primary peaks at around 25° and 43° respectively, which are assigned to the (002) and the (101) planes of the graphite carbon crystal structure. No obvious diffraction peaks of Fe or its oxides/carbides/nitrides can be detected in the XRD spectra, confirming the absence of highly crystalline Fe-containing species. These results are consistent with the TEM and HAADF images (Fig. 1), indicating the single Fe atoms in Fe-N-C-800 catalyst.

Moreover, Raman spectroscopy was employed to probe the graphitization degree of these catalysts. As presented in Fig. 2b, all of the catalysts present two distinct peaks at around 1345 and 1590 cm^{-1}, which are designated as the D-band for lattice defects and G-band peaks for sp^2-hybridized carbon, respectively.18 The calculated I_D/I_G ratio of Fe-N-C-800 catalyst is 1.03, which is slightly higher than Fe-Phen-C (1.01), Fe-Urea-C (0.95) and N-C (0.93), respectively, indicating that more defects were created in the carbon matrix due to the introduction of Fe and dual N precursors. The specific surface area and pore textures of Fe-N-C-800 was characterized by nitrogen adsorption-desorption isotherm, as depicted in Fig. 2c. Interestingly, the Fe-N-C-800 catalyst exhibits the type IV isotherm with a relatively high specific surface area of 487 m^2 g^{-1}, much higher than Fe-Phen-C (114 m^2 g^{-1}). Noteworthily, the specific surface area of Fe-Urea-C is up to 752 m^2 g^{-1}. Moreover, the Fe-N-C-800 exhibits a pore volume of 1.31 cm^3 g^{-1}, substantially surpassing the Fe-Phen-C (0.61 cm^3 g^{-1}), which indicates that urea plays a crucial role in enlarging the specific surface area and porosity. Urea decomposes at high temperatures to generate melamine and some gases, e.g. CO_2 and NH_3. The gases apparently promote the formation of pores, resulting in an enhanced specific surface area and increased porosity. The pore size distribution of all catalysts is mainly concentrated around 4 nm (Fig. 2d), demonstrating that the dominant mesoporous structures were formed in the pyrolysis process. Such a porous structure likely exposes more catalytic active sites and promote the efficient mass transfer of reactants, products and electrons during the ORR process.[29,39]

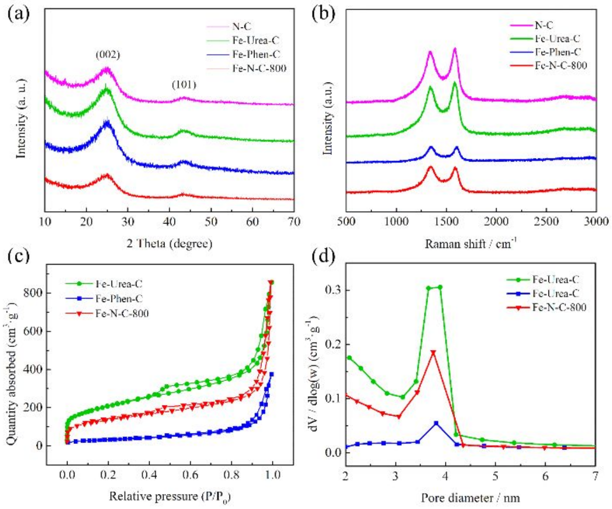

Fig. 2 (a) XRD spectra and (b) Raman spectra of N-C, Fe-Urea-C, Fe-Phen-C and Fe-N-C-800. (c) Nitrogen adsorption-desorption isotherm and (d) the enlarged pore size distribution of Fe-Urea-C, Fe-Phen-C and Fe-N-C-800.

In order to investigate the surface chemistry of all the catalysts, X-ray photoelectron spectroscopy (XPS) was performed as depicted in Fig. 3. The wide spectra indicate the coexistence of C, N and O in all catalysts (Fig. S10). It is noteworthy that the signals of iron cannot be detected likely due to the limited detection. The contents of elements based on XPS spectra are listed in Table S1. The deconvoluted XPS spectra of narrow C1s peaks for different catalysts are shown in

Fig. S11. Four detailed peaks including C-C (284.75 eV), C-N (285.51 eV), C-O (286.58 eV) and C=O (289.40 eV) are observed, respectively,[40-42] implying the successful doping of N atoms in the carbon matrix.

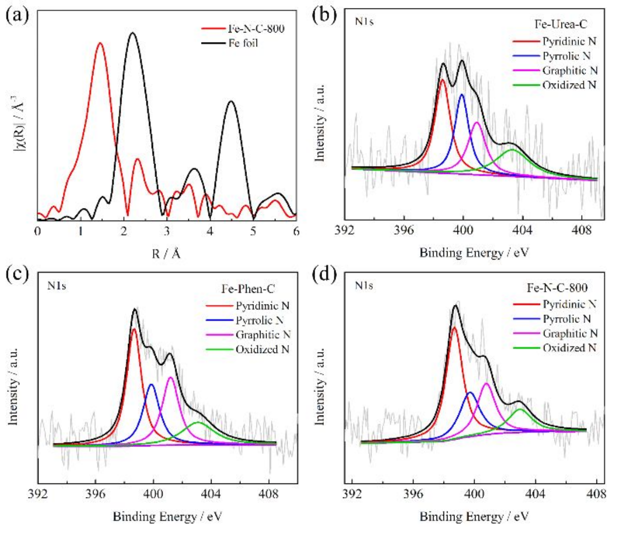

Fig. 3 (a) Fourier transforms of the Fe K-edge EXAFS spectra for Fe-N-C-800 and Fe foil (the data of Fe foil is reproduced from Ref. [45]) (c) High-resolution N 1s XPS spectra of Fe-Phen-C. (d) High-resolution N 1s XPS spectra of Fe-N-C-800.

To intuitively identify the coordination environment of iron atoms in Fe-N-C-800, extended X-ray absorption fine structure (EXAFS) at the Fe K-edge was performed. As shown in Fig. 3a, the Fe K-edge EXAFS spectra exhibit a dominated peak at 1.44 Å, which is assigned to Fe-N bond,[43,44] corroborating that the iron atoms mainly exist in the form of Fe-Nx moieties in the carbon matrix. In addition, the peak position for Fe-N-C-800 catalyst in the second coordination sphere (2.3 Å) is slightly different from the Fe-Fe bond in standard Fe foil.[45] Due to the extremely low Fe content in the catalyst (1.09 wt%) and detailed analysis in Ref. [46], this peak can be assigned to Fe-C bond.[46] Given that the peak intensity of Fe-N-C-800 at 2.3 Å is much lower than the peak at 1.44 Å (Fe-Nx moieties), it is strongly supported that the Fe in Fe-N-C-800 sample primarily exists in the form of Fe-Nx, even though the other trace of Fe element exsit in the form of Fe-C.

On the other hand, The high-resolution N 1s spectra for all prepared catalysts are deconvoluted to pyridinic N (398.6±0.2 eV), pyrrolic N (399.9±0.2 eV), graphitic N (401.0±0.2 eV) and oxidized N (402~404 eV), respectively (Fig. 3b, c and d).[30,47] It is worth noting that the peak located at 398.6 (±0.2 eV) can also be assigned to Fe-N because of the negligible difference in binding energy between pyridinic-N and Fe-N.[48,49] Given that the EXAFS spectra show considerable Fe-N signals, this peak could be assigned to the overlapped pyridinic-N and Fe-N. Nitrogen contents of Fe-Urea-C, Fe-Phen-C and Fe-N-C-800 were determined to be 0.97 at%, 1.52 at% and 2.39 at%, respectively (Table S1), indicating that the dual nitrogen sources could promote nitrogen doping after the pyrolysis. Furthermore, the high content of pyridinic N is favorable for the formation of Fe-Nx moieties.[50-52] The ratio of pyridinic N/Fe-N in Fe-N-C-800 (44.00%) is remarkably higher than Fe-Phen-C (37.60%) and Fe-Urea-C (32.75%) (Table S2), demonstrating the presence of rich pyridinic N in the Fe-N-C-800. It could be speculated that Phen and urea can jointly promote the formation of pyridinic N and further abundant Fe-Nx moieties, agreeing well with the EXAFS results. However, Fe 2p signal of Fe-N-C-800 could not be detected clearly (Fig. S11d), probably owing to the low Fe content on the near-surface,[53,54] only 1.09 wt% measured in Fe-N-C-800 by inductively coupled plasma optical emission spectrometry (ICP-OES). It still overpasses the Fe-Phen-C (0.86 wt%) and Fe-Urea-C (0.60 wt%), agreeing well with the results of the fitted N 1s spectra (Fig. 3), which confirms that dual nitrogen sources are beneficial to synergistically stimulate the formation of more Fe-Nx moieties.

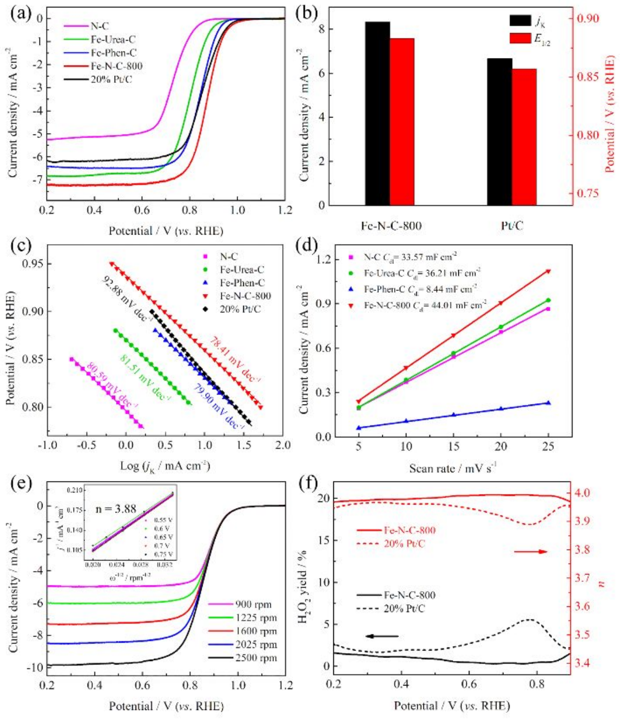

Fig. 4 (a) ORR polarization curves of N-C, Fe-Urea-C, Fe-Phen-C, Fe-N-C-800 and 20% Pt/C in 0.1 M KOH. (b) j_K at 0.85 V and $E_{1/2}$ for Fe-N-C-800 and commercial Pt/C. (c) Tafel plots for N-C, Fe-Urea-C, Fe-Phen-C, Fe-N-C-800 and 20% Pt/C. (d) Plots of current densities (at 1.1 V vs. RHE) as a function of scan rates. (e) ORR polarization curves at different rotating rates (inset: the fitted K-L plots and electron transfer numbers) (f) Peroxide yields and the electron transfer numbers (n) for Fe-N-C-800 and 20% Pt/C.

The ORR performances of the as-synthesized catalysts were performed in 0.1 M KOH solution. As presented in Fig. 4a, the N-C catalyst without iron precursor exhibits the lowest ORR activity in terms of onset potential (E_{onset}) of 0.887 V and half-wave potential ($E_{1/2}$) of 0.721 V, indicating that the introduction of iron plays a critical role in enhancing the ORR activity. The dual-nitrogen-source derived Fe-N-C-800 exhibits an apparently enhanced activity, e.g. the $E_{1/2}$ at 0.883 V, 32 mV and 72 mV higher than Fe-Phen-C ($E_{1/2}$=0.851 V), Fe-Urea-C ($E_{1/2}$=0.811 V), the commercial Pt/C ($E_{1/2}$=0.857 V), and recently reported Fe-N-C ORR electrocatalysts (Table S3), respectively. These results suggest that dual nitrogen sources would substantially boost the ORR activity. The performance of Fe-N-C-800 was also evaluated in the acidic O_2-saturated 0.1 M $HClO_4$ solution. An $E_{1/2}$ of 0.723 V is obtained (Fig. S12). Although this performance is slightly lower than Pt/C by approximately 60 mV, it presents a moderate ORR activity compared with previously reported Fe-based catalysts in acidic media (Table S4).

Beyond the simple half-wave potential, the kinetic current density (j_k) of Fe-N-C-800 is calculated as 8.32 mA cm^{-2} at 0.85 V, higher than that of commercial Pt/C (6.67 mA cm^{-2}) (Fig. 4b). As shown in Fig. 4c, the Tafel slope of Fe-N-C-800 catalyst is 78.41 mV dec^{-1}, smaller than other catalysts and even the commercial Pt/C, which reveals a more efficient kinetic process of oxygen reduction on Fe-N-C-800. Moreover, the electrochemical surface area (ECSA) was assessed by the double layer capacitance (C_{dl}), which was performed by cyclic voltammetry with a series of different scan rates from 5 mV s^{-1} to 25 mV s^{-1} (Fig. 4d and Fig. S13). The C_{dl} of Fe-N-C-800 catalyst is 44.01 mF cm^{-2}, much higher than Fe-Phen-C (8.84 mF cm^{-2}), Fe-Urea-C (36.21 mF cm^{-2}) and N-C (33.57 mF cm^{-2}), respectively.

To investigate the reaction pathway of Fe-N-C-800, the polarization curves at different rotation rates from 900 to 2500 rpm were presented in Fig. 4e. Meanwhile, the fitted Koutecky-Levich (K-L) plots (inset of Fig. 4e) at different potentials were obtained according to K-L equation. The electron transfer number is reasonably calculated to be approximately 3.88, suggesting a more favorable four-electron transfer process.

Rotating ring-disk electrode (RRDE) tests were employed to further measure the hydrogen peroxide yield (H_2O_2%) and electron transfer number, as shown in Fig. 4f. The H_2O_2% of Fe-N-C-800 is no more than 2% at the potential from 0.2 V to 0.9 V, apparently lower than that of the commercial Pt/C. Once again, the Fe-N-C-800 catalyst follows an almost four-electron transfer process in terms of the electron transfer number of 3.95~4.0, which is consistent with the aforementioned results (Fig. 4e). Based on the above facts, the dual nitrogen sources derived Fe-N-C-800 delivered superior activity toward ORR.

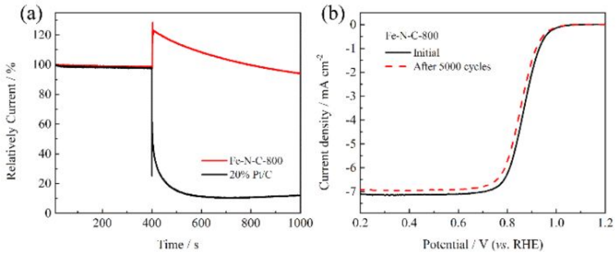

Fig. 5 (a) Chronoamperometric response with methanol of Fe-N-C-800 and 20% Pt/C at 0.75 V under rotation speed of 1600 rpm. (b) ORR polarization curves before and after 5000 cycles of Fe-N-C-800 at 1600 rpm with a scan rate of 10 mV s^{-1}.

The methanol tolerance and stability of Fe-N-C-800 were also evaluated through chronoamperometry current-time (*i-t*) curves and accelerated durability test (ADT). As shown in Fig. 5a, the *i-t* curves were carried out at 0.75 V for 1000 s with a rotation of 1600 rpm in O_2-saturated 0.1 M KOH electrolyte. Obviously, the current sharply declines while injecting methanol into the electrolyte at 400th second. Impressively, the current of Fe-N-C-800 remains 94% after 1000 s, substantially surpassing the commercial Pt/C (12%), indicating that Fe-N-C-800 shows superior tolerance to methanol. The stability is also an important index to assess whether the catalyst can be used for a long time in practical production. The ORR polarization curves were examined before and after 5000 cycles from 0.6 V to 1.0 V with a scan rate of 50 mV s^{-1} in O_2-saturated 0.1 M KOH solution (Fig. 5b). Apparently, the ORR performance of Fe-N-C-800 only decays 13 mV after 5000 cycles, much lower than that of the commercial Pt/C (34 mV) (Fig. S14), demonstrating that Fe-N-C-800 exhibits outstanding long-term stability.

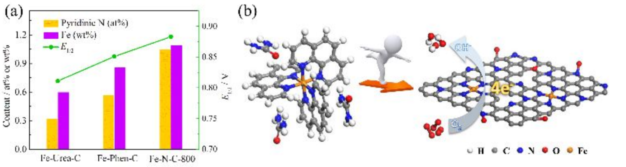

Fig. 6 (a) Relations between the content of pyridinic N and Fe with $E_{1/2}$ for Fe-Urea-C, Fe-Phen-C and Fe-N-C-800. (b)The schematic diagram and microstructure of urea and Fe-Phen complex.

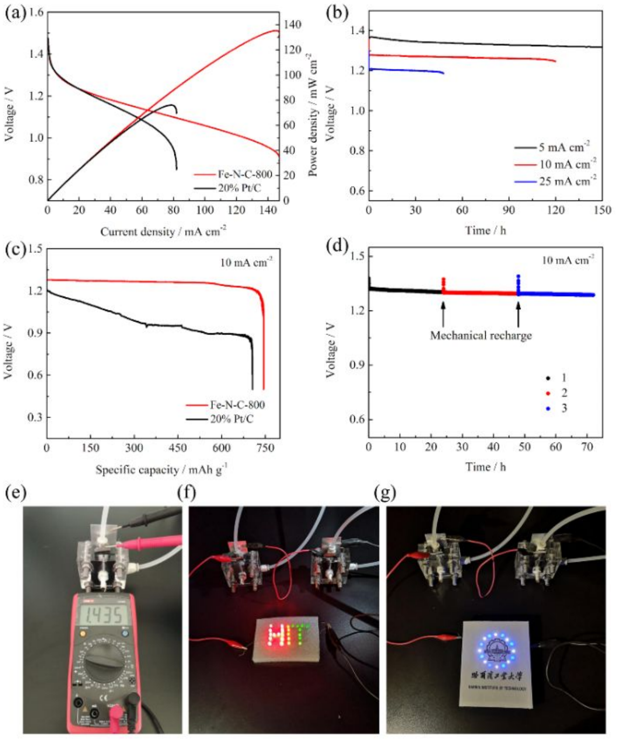

Fig. 7 (a) Polarization and corresponding power density curves of primary Zn-air batteries using Fe-N-C-800 and 20% Pt/C catalysts at a scan rate of 5 mV s^{-1}. (b) Discharge curves of Fe-N-C-800 based primary Zn-air batteries at various current densities. (c) Specific capacities of the Zn-air batteries using various ORR catalysts at 10 mA cm^{-2}, which is normalized to the mass of the consumed Zn. (d) Long-term durability tests of the Fe-N-C-800 based primary Zn-air battery with mechanical recharge at 10 mA cm^{-2}. (e) Photograph of primary Zn-air battery exhibiting a minimum open-circuit voltage of ≈1.435 V measured with a multimeter. (f-g) Photographs of lighted LEDs powered by two Zn-air batteries in series based on Fe-N-C-800.

It is interesting that the content of pyridinic N and Fe have a linear relationship with the ORR activity in terms of $E_{1/2}$, respectively (Fig. 6a). Compared with Fe-Urea-C and Fe-Phen-C, the content of pyridinic N and Fe are both significantly increased in Fe-N-C-800. Meanwhile, the $E_{1/2}$ of Fe-N-C-800 is shifted more positive, which suggests that the introduction of dual nitrogen sources can effectively enhance the ORR activity. As shown in Fig. 6b, Fe^{2+} could preferentially combine with Phen to form a stable hexadentate coordination complex due to the strong affinity between Phen and Fe^{2+}. Therefore, a typical octahedral configuration generates with an iron ion surrounded by three Phen molecules connected with Fe and N. The huge ligands of Phen molecules are hypothesized to lead to steric hindrance effect and efficiently protect Fe atoms from aggregation. It is noteworthy that the urea molecule is one of the smallest N precursors so that it can be controllably inserted into the space of the complex. The dual N precursors including Phen and urea would provide abundant N to coordinate with Fe, in contrast to the cases using individual Phen or urea as N precursor. The strong coordination between Fe^{2+} and Phen, and abundant N in urea are synergistically assistant in the well-defined formation of Fe-Nx moieties.

To evaluate practical application of the Fe-N-C-800 catalyst, the primary Zn-air batteries were assembled by using zinc foil as anode electrode, and Fe-N-C-800 catalyst (2.0 mg cm^{-2}) as air cathode. For comparison, the 20% Pt/C catalyst was employed at cathode with the same loading. The assembled Zn-air battery displays a high open-circuit voltage of 1.476 V with Fe-N-C-800, extremely close to that of Pt/C (1.48 V) (Fig.7a). Interestingly, the peak-power density of the battery using Fe-N-C-800 catalyst at cathode is 135.3 mW cm^{-2}, much higher than Pt/C (76.1 mW cm^{-2}), and even those of reported advanced catalysts (Table S5). Subsequently, the galvanostatic discharge curves of Zn-air battery with Fe-N-C-800 at various current densities were tested, as shown in Fig.7b. Such a PGM-free Zn-air battery demonstrates stable galvanostatic discharge curves at 5 mA cm^{-2} for ~150 h, 10 mA cm^{-2} for ~120 h and 25 mA cm^{-2} for ~48 h, respectively, indicating the superior stability. The specific capacity normalized to the mass of consumed Zn at 10 mA cm^{-2} is 744 $mAh{\cdot}g_{Zn}^{-1}$ for the Fe-N-C-800 based battery, corresponding to a gravimetric energy density of 940 $Wh{\cdot}g_{Zn}^{-1}$, which significantly exceeds the Pt/C based battery (706 $mAh{\cdot}g_{Zn}^{-1}$) (Fig.7c). Gratifyingly, it can be seen from Fig.7d that the battery using Fe-N-C-800 as cathode could be mechanically recharged for several cycles by replacing Zn foil and electrolyte, enabling continuous discharge for over 72 h at a current density of 10 mA cm^{-2}, which suggests a long-term lifetime of Fe-N-C-800 as a ORR catalyst. As depicted in Fig.7e, it is observed that the PGM-free battery displays a high open-circuit voltage of 1.435 V measured with a multimeter. To further demonstrate the potential feasibility in some practical power devices, two Zn-air batteries were connected in series to supply adequate voltage to power several different colored LEDs (5 mm, 2.5 V) (Fig.7f and 7g), and other small power devices, e.g. fans (2.5 V) (Video S1). These results demonstrate the great potential of dual-nitrogen-source engineered Fe-N-C-800 catalyst in the air cathode for high power Zn-air batteries.

Conclusions

In summary, a synthesis strategy using the synergistic effect of dual nitrogen sources is designed to achieve a highly efficient oxygen reduction catalyst. On the one hand, the Phen would anchor the iron atom via strong hexadentate coordination; on the other hand, the urea could insert into the space of the Fe-Phen complex due to its smaller size. The constructed three-dimensional spatial geometric structure would effectively anchor and separate the iron atom to form active Fe-Nx moieties. The optimized Fe-N-C-800 shows high ORR activity with a half-wave potential of 0.883V and also displays outstanding stability and methanol tolerance, which is superior to the commercial Pt/C. Furthermore, the primary Zn-air batteries based on Fe-N-C-800 display a high specific capacity as well as a desirable stability. The synthesis strategy using the synergistic effect of dual nitrogen sources is highly desirable, which could be promisingly applied in the preparation of other NPMCs besides the Fe-N-C catalysts.

Conflicts of interest

There are no conflicts to declare.

Acknowledgements

The authors gratefully acknowledge financial support from the National Natural Science Foundation of China (Grant No. 21878061 and Grant No. 21805064). This research used resources of the Advanced Photon Source, an Office of Science User Facility operated for the U.S. Department of Energy (DOE) Office of Science by Argonne National Laboratory, and was supported by the U.S. DOE under Contract No. DE-AC02-06CH11357, and the Canadian Light Source and its funding partners.

References

1 J. Lee, S. Tai Kim, R. Cao, N. Choi, M. Liu, K. T. Lee and J. Cho, *Adv. Energy Mater.*, 2011, **1**, 34-50.
2 M. K. Debe, *Nature*, 2012, **486**, 43-51.
3 Z. L. Wang, D. Xu, J. J. Xu and X. B. Zhang, *Chem. Soc. Rev.*, 2014, **43**, 7746-7786.
4 Z. W. Seh, J. Kibsgaard, C. F. Dickens, I. Chorkendorff, J. K. Nørskov and T. F. Jaramillo, *Science*, 2017, **355**, d4998.
5 L. Du, Y. Shao, J. Sun, G. Yin, J. Liu and Y. Wang, *Nano Energy*, 2016, **29**, 314-322.
6 L. Du, S. Zhang, G. Chen, G. Yin, C. Du, Q. Tan, Y. Sun, Y. Qu and Y. Gao, *ACS Appl. Mater. Inter.*, 2014, **6**, 14043-14049.
7 L. Du, C. Du, G. Chen, F. Kong, G. Yin and Y. Wang, *ACS Appl. Mater. Inter.*, 2016, **8**, 15250-15257.
8 M. Lefevre, E. Proietti, F. Jaouen and J. P. Dodelet, *Science*, 2009, **324**, 71-74.
9 S. Guo and S. Sun, J. Am. Chem. Soc., 2012, 134, 2492-2495.
10 A. Song, L. Cao, W. Yang, Y. Li, X. Qin and G. Shao, *ACS Sustain. Chem. Eng.*, 2018, **6**, 4890-4898.
11 S. Wang, Q. He, C. Wang, H. Jiang, C. Wu, S. Chen, G. Zhang and L. Song, *Small*, 2018, **14**, 1800128.
12 D. Liu, C. Wu, S. Chen, S. Ding, Y. Xie, C. Wang, T. Wang, Y. A.

Haleem, Z. Ur Rehman, Y. Sang, Q. Liu, X. Zheng, Y. Wang, B. Ge, H. Xu and L. Song, *Nano Res.*, 2018, **11**, 2217-2228.

13 Q. Wang, Y. Lei, Z. Chen, N. Wu, Y. Wang, B. Wang and Y. Wang, *J. Mater. Chem. A*, 2018, **6**, 516-526.

14 X. Yan, K. Liu, T. Wang, Y. You, J. Liu, P. Wang, X. Pan, G. Wang, J. Luo and J. Zhu, *J. Mater. Chem. A*, 2017, **5**, 3336-3345.

15 X. Chen, L. Yu, S. Wang, D. Deng and X. Bao, *Nano Energy*, 2017, **32**, 353-358.

16 G. Wu, K. L. More, C. M. Johnston and P. Zelenay, *Science*, 2011, **332**, 443-447.

17 X. X. Wang, D. A. Cullen, Y. Pan, S. Hwang, M. Wang, Z. Feng, J. Wang, M. H. Engelhard, H. Zhang, Y. He, Y. Shao, D. Su, K. L. More, J. S. Spendelow and G. Wu, *Adv. Mater.*, 2018, **30**, 1706758.

18 I. S. Amiinu, X. Liu, Z. Pu, W. Li, Q. Li, J. Zhang, H. Tang, H. Zhang and S. Mu, *Adv. Funct. Mater.*, 2018, **28**, 1704638.

19 H. Wu, H. Li, X. Zhao, Q. Liu, J. Wang, J. Xiao, S. Xie, R. Si, F. Yang, S. Miao, X. Guo, G. Wang and X. Bao, *Energy Environ. Sci.*, 2016, **9**, 3736-3745.

20 M. Xiao, J. Zhu, L. Ma, Z. Jin, J. Ge, X. Deng, Y. Hou, Q. He, J. Li, Q. Jia, S. Mukerjee, R. Yang, Z. Jiang, D. Su, C. Liu and W. Xing, *ACS Catal.*, 2018, **8**, 2824-2832.

21 A. Han, W. Chen, S. Zhang, M. Zhang, Y. Han, J. Zhang, S. Ji, L. Zheng, Y. Wang, L. Gu, C. Chen, Q. Peng, D. Wang and Y. Li, *Adv. Mater.*, 2018, **30**, 1706508.

22 J. Li, Y. Song, G. Zhang, H. Liu, Y. Wang, S. Sun and X. Guo, *Adv. Funct. Mater.*, 2017, **27**, 1604356.

23 Y. Hu, J. O. Jensen, W. Zhang, L. N. Cleemann, W. Xing, N. J. Bjerrum and Q. Li, *Angew. Chem., Int. Ed.*, 2014, **53**, 3675-3679.

24 X. Wang, H. Zhang, H. Lin, S. Gupta, C. Wang, Z. Tao, H. Fu, T. Wang, J. Zheng, G. Wu and X. Li, *Nano Energy*, 2016, **25**, 110-119.

25 L. Ma, S. Chen, Z. Pei, Y. Huang, G. Liang, F. Mo, Q. Yang, J. Su, Y. Gao, J. A. Zapien and C. Zhi, *ACS Nano*, 2018, **12**, 1949-1958.

26 Y. Chen, S. Ji, Y. Wang, J. Dong, W. Chen, Z. Li, R. Shen, L. Zheng, Z. Zhuang, D. Wang and Y. Li, *Angew. Chem., Int. Ed.*, 2017, **56**, 6937-6941.

27 Q. Li, W. Chen, H. Xiao, Y. Gong, Z. Li, L. Zheng, X. Zheng, W. Yan, W. Cheong, R. Shen, N. Fu, L. Gu, Z. Zhuang, C. Chen, D. Wang, Q. Peng, J. Li and Y. Li, *Adv. Mater.*, 2018, **30**, 1800588.

28 M. Sun, D. Davenport, H. Liu, J. Qu, M. Elimelech, J. Li, *J. Mater. Chem. A*, 2018, **6**, 2527-2539.

29 C. Zhang, J. Liu, Y. Ye, Z. Aslam, R. Brydson and C. Liang, *ACS Appl. Mater. Inter.*, 2018, **10**, 2423-2429.

30 L. Lin, Q. Zhu and A. Xu, *J. Am. Chem. Soc.*, 2014, **136**, 11027-11033.

31 L. Du, Y. Shao, J. Sun, G. Yin, C. Du and Y. Wang, *Catal. Sci. Technol.*, 2018, **8**, 3216-3232.

32 Q. Lai, L. Zheng, Y. Liang, J. He, J. Zhao and J. Chen, *ACS Catal.*, 2017, **7**, 1655-1663.

33 Z. K. Yang, Z. Zhao, K. Liang, X. Zhou, C. Shen, Y. Liu, X. Wang and A. Xu, *J. Mater. Chem. A*, 2016, **4**, 19037-19044.

34 E. Proietti, F. Jaouen, M. Lefèvre, N. Larouche, J. Tian, J. Herranz and J. Dodelet, *Nat. Commun.*, 2011, **2**.

35 L. Osmieri, R. Escudero-Cid, M. Armandi, A. H. A. Monteverde Videla, J. L. García Fierro, P. Ocón and S. Specchia, *Appl. Catal. B Environ.*, 2017, **205**, 637-653.

36 H. T. Chung, D. A. Cullen, D. Higgins, B. T. Sneed, E. F. Holby, K. L. More and P. Zelenay, *Science*, 2017, **357**, 479-484.

37 N. A. M. Barakat, A. G. El-Deen, Z. K. Ghouri and S. Al-Meer, *Sci. Rep.*, 2018, **8**.

38 X. Bai, Y. Shi, J. Guo, L. Gao, K. Wang, Y. Du and T. Ma, *J. Power Sources*, 2016, **306**, 85-91.

39 Z. K. Yang, L. Lin and A. Xu, *Small*, 2016, 12, 5710-5719.

40 S. Song, Y. Xue, L. Feng, H. Elbatal, P. Wang, C. N. Moorefield, G. R. Newkome and L. Dai, *Angew. Chem., Int. Ed.*, 2014, **53**, 1415-1419.

41 G. Ren, L. Gao, C. Teng, Y. Li, H. Yang, J. Shui, X. Lu, Y. Zhu and L. Dai, *ACS Appl. Mater. Inter.*, 2018, **10**, 10778-10785.

42 Y. Li, W. Zhou, H. Wang, L. Xie, Y. Liang, F. Wei, J. Idrobo, S. J. Pennycook and H. Dai, *Nat. Nanotech.*, 2012, **7**, 394-400.

43 S. Liang, R. Chen, P. Yu, M. Ni, Q. Zhang, X. Zhang and W. Yang, *Chem. Commun.*, 2017, **53**, 11453-11456.

44 K. Yuan, S. Sfaelou, M. Qiu, D. Lützenkirchen-Hecht, X. Zhuang, Y. Chen, C. Yuan, X. Feng and U. Scherf, *ACS Energy Lett.*, 2017, **3**, 252-260.

45 L. Du, L. Luo, Z. Feng, M. Engelhard, X. Xie, B. Han, J. Sun, J. Zhang, G. Yin, C. Wang, Y. Wang and Y. Shao, *Nano Energy*, 2017, **39**, 245-252.

46 H. Fei, J. Dong, Y. Feng, C. S. Allen, C. Wan, B. Volosskiy, M. Li, Z. Zhao, Y. Wang, H. Sun, P. An, W. Chen, Z. Guo, C. Lee, D. Chen, I. Shakir, M. Liu, T. Hu, Y. Li, A. I. Kirkland, X. Duan and Y. Huang, *Nat. Catal.*, 2018, **1**, 63-72.

47 Y. Ding, Y. Niu, J. Yang, L. Ma, J. Liu, Y. Xiong and H. Xu, *Small*, 2016, **12**, 5414-5421.

48 H. Liang, W. Wei, Z. Wu, X. Feng and K. Müllen, *J. Am. Chem. Soc.*, 2013, **135**, 16002-16005.

49 G. Wu, C. M. Johnston, N. H. Mack, K. Artyushkova, M. Ferrandon, M. Nelson, J. S. Lezama-Pacheco, S. D. Conradson, K. L. More, D. J. Myersd and P. Zelenay, *J. Mater. Chem.*, 2011, **21**, 11392-11405.

50 H. R. Byon, J. Suntivich and Y. Shao-Horn, *Chem. Mater.*, 2011, **23**, 3421-3428.

51 A. Kong, X. Zhu, Z. Han, Y. Yu, Y. Zhang, B. Dong and Y. Shan, *ACS Catal.*, 2014, **4**, 1793-1800.

52 S. Yasuda, A. Furuya, Y. Uchibori, J. Kim and K. Murakoshi, *Adv. Funct. Mater.*, 2016, **26**, 738-744.

53 H. Shen, E. Gracia-Espino, J. Ma, H. Tang, X. Mamat, T. Wagberg, G. Hu and S. Guo, *Nano Energy*, 2017, **35**, 9-16.

54 C. Zhu, S. Fu, J. Song, Q. Shi, D. Su, M. H. Engelhard, X. Li, D. Xiao, D. Li, L. Estevez, D. Du and Y. Lin, *Small*, 2017, **13**, 1603407.

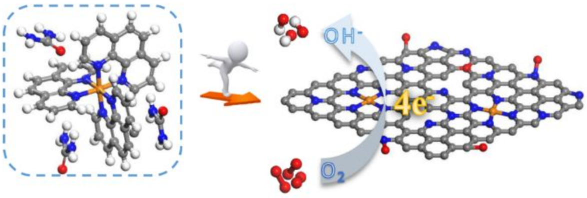

The improved ORR performance is attributed to rich density of the Fe-Nx moieties derived from regulated coordination structures by dual-nitrogen-source.